PHYSICAL REVIEW B **95**, 201402(R) (2017)

Monolayer of the 5*d* transition metal trichloride $OsCl_3$: A playground for two-dimensional magnetism, room-temperature quantum anomalous Hall effect, and topological phase transitions

Xian-Lei Sheng[1,2] and Branislav K. Nikolić[1,*]

[1]*Department of Physics and Astronomy, University of Delaware, Newark, Delaware 19716-2570, USA*

[2]*Department of Applied Physics, Beihang University, Beijing 100191, China*

(Received 9 October 2016; revised manuscript received 20 February 2017; published 3 May 2017)

Based on density functional theory (DFT) calculations, we predict that a monolayer of $OsCl_3$ (which is a layered material whose interlayer coupling is weaker than in graphite) possesses a quantum anomalous Hall (QAH) insulating phase generated by the combination of honeycomb lattice of osmium atoms, their strong spin-orbit coupling (SOC), and ferromagnetic ground state with *in-plane* easy axis. The band gap opened by SOC is $E_g \simeq 67$ meV (or $\simeq 191$ meV if the easy axis can be tilted out of the plane by an external electric field), and the estimated Curie temperature of such an *anisotropic planar rotator* ferromagnet is $T_C \lesssim 350$ K. The Chern number $\mathcal{C} = -1$, generated by the manifold of Os t_{2g} bands crossing the Fermi energy, signifies the presence of a single chiral edge state in nanoribbons of finite width, where we further show that edge states are spatially narrower for zigzag than armchair edges and investigate edge-state transport in the presence of vacancies at Os sites. Since 5*d* electrons of Os exhibit *both* strong SOC and moderate correlation effects, we employ DFT+U calculations to show how increasing on-site Coulomb repulsion U: gradually reduces E_g while maintaining $\mathcal{C} = -1$ for $0 < U < U_c$, leads to a metallic phase with $E_g = 0$ at U_c, and opens a gap of topologically trivial Mott insulating phase with $\mathcal{C} = 0$ for $U > U_c$.

DOI: 10.1103/PhysRevB.95.201402

Introduction. The quantum anomalous Hall (QAH) insulator is a recently discovered [1,2] topological electronic phase where strong spin-orbit coupling (SOC) and ferromagnetic ordering conspire to generate band gap E_g in the bulk of a two-dimensional (2D) electron system, as well as conducting (i.e., gapless) chiral edge states at its boundaries. Its topologically nontrivial band structure is characterized by a nonzero Chern number $\mathcal{C}$ counting the number edge states whose energy-momentum dispersion threads the gap of finite-width wires, while their wave functions have finite spatial extent around the wire edges. Experimental confirmation of QAH insulators is based on the observation of quantized Hall conductance in the absence of any external magnetic field [2].

Unlike a closely related quantum Hall (QH) insulator, where chiral edge states allow a spin-unpolarized electron to propagate in only one direction, or quantum spin Hall (QSH) insulator, where helical edge states appear in pairs with different chirality and spin polarization [3], the edge states of QAH insulator allow only one spin species to flow unidirectionally. Thus, the edge state transport in nanowires made of QAH insulator is robust against *both* magnetic and nonmagnetic disorder, which makes them superior to edge states of QSH insulator where electrons can be backscattered by disorder (such as magnetic impurities) breaking the time-reversal symmetry. The QAH insulator is also superior in potential applications to QH insulator since the latter requires large external magnetic field and low temperatures.

However, QAH insulators have been observed thus far only at very low temperatures $\lesssim 100$ mK [1,2], thereby igniting intense theoretical and computational searches [4] for systems whose *both* E_g/k_B and the Curie temperature T_C are higher than the room temperature. Finding such materials, or heterostructures of different materials [5,6], would open new avenues for nanoelectronic and spintronic devices with ultralow dissipation where edge states act as "chiral interconnects" whose resistance is independent of the length of the wire [1].

The seminal work on the Haldane model [7], where quantized Hall conductance is found for an electronic system defined on the honeycomb lattice with SOC in the absence of an external magnetic field, has inspired search for realistic materials exhibiting QSH or QAH insulating states where the honeycomb lattice structure is often the first ingredient [8,9]. For example, graphene with enhanced intrinsic SOC [3,10,11] can be transformed into QSH insulator and then converted into QAH insulator by adding exchange magnetic field (via impurities, doping, or proximity effect) in order to suppress one of the two helical edge states of the QSH insulator. Systems predicted to realize this concept include

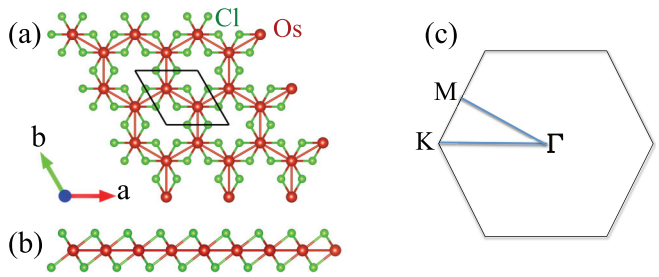

FIG. 1. (a) Top and (b) side view of the crystalline structure of monolayer $OsCl_3$ where a sheet of transition metal Os atoms is sandwiched between two sheets of Cl atoms. The Os atoms form a honeycomb lattice, and each Os atom is located at an octahedral site between the Cl atom sheets. (c) First Brillouin zone of monolayer $OsCl_3$ with the high symmetry points indicated.

*bnikolic@udel.edu

 ©2017 American Physical Society

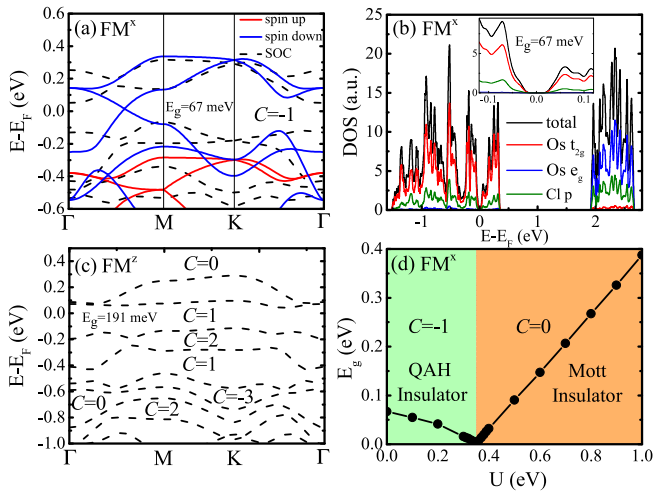

FIG. 2. Electronic band structure of monolayer $OsCl_3$ with Os spins in the: (a) in-plane FM^x configuration shown in Fig. 4(a) and (c) out-of-plane FM^z configuration (see also Table II). The band structure is computed with GGA (solid lines) or GGA+SOC (dashed lines). (b) Density of states corresponding to panel (a). (d) The phase diagram of $OsCl_3$ with Os spins in the FM^x configuration calculated by GGA+SOC+U.

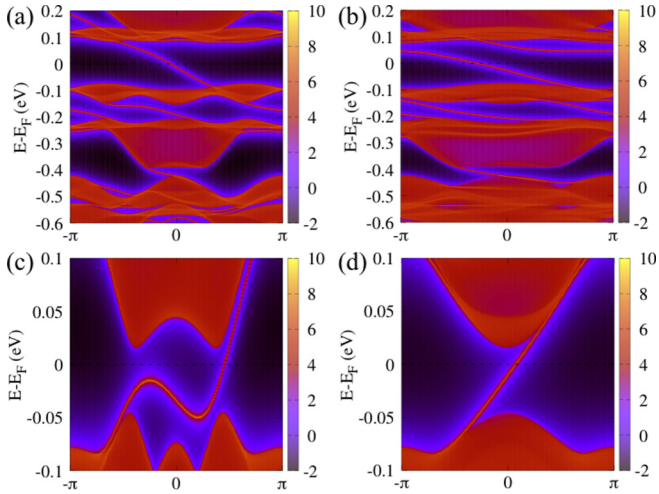

FIG. 3. Energy and k_x dependence of the local DOS on the edge of a semi-infinite sheet of $OsCl_3$ which is terminated by either (a),(c) zigzag or (b),(d) armchair arrangement of Os atoms along the edge. The Os spins are in FM^z configuration in (a) and (b) or FM^x configuration [illustrated in Fig. 4(a)] in (c) and (d). Warmer colors represent higher local DOS, where solid red regions indicate bulk energy bands and the blue regions indicate bulk energy gap.

graphene decorated with heavy 5*d* transition metal adatoms [12] or heterostructures like graphene/antiferromagnet [5] and graphene/ferromagnetic-insulator [6,13]. The proximity SOC in graphene can be further enhanced by inserting a monolayer of transition metal dichalcogenides (TMD) into such heterostructures [11]. Similarly, honeycomb lattices of silicene, germanene, and stanene, which already possess strong intrinsic SOC, could be converted into QAH insulator by introducing exchange interaction via magnetic adatoms [14] or surface functionalization [8]. Finally, a honeycomb lattice enforcing trigonal symmetry of the crystalline field can introduce additional level splitting of the *d* orbitals, which combined with SOC makes possible opening of topological gaps in transition metal oxide heterostructures [9,15]. However, all of the heterostructures mentioned above have E_g below room temperature, thereby requiring strain engineering or external pressure to increase E_g [5]. Also, despite numerous predictions [10,12,14] for topological phases in graphene decorated with heavy adatoms none has been realized thus far (in part, due to difficulties in keeping adatoms sufficiently apart from each other [16,17]).

Thus, recent efforts [4,18] have also focused on the possibility of *intrinsic* QAH insulator realized in ferromagnetic insulating materials which are, however, quite rare at room temperature [1]. In this Rapid Communication, we predict that monolayer $OsCl_3$ possesses an intrinsic QAH insulating phase characterized by: an energy gap $E_g \simeq 67$ meV, opened only when SOC is turned on in our density functional theory (DFT) calculations; a Chern number $|\mathcal{C}| = 1$, which (i.e., the corresponding number of edge states per boundary) can be increased by tuning the Fermi energy E_F; and an estimated Curie temperature $T_C \lesssim 350$ K. We emphasize that E_g of $OsCl_3$ is *much larger* than recently predicted $E_g \simeq 20$ meV of the intrinsic QAH insulator in monolayer kagome lattice $Cs_2Mn_3F_{12}$ [18] or $E_g \simeq 25$ meV for LaX (X=Br, Cl, and I) compounds [4]. In addition, accurate estimates of T_C for such low-dimensional magnets, which take into account magnetocrystalline anisotropy (MCA) induced by strong SOC, are lacking.

The layered nature of several transition metal trichlorides MCl_3—where M = Ti, V, Cr, Fe, Mo, Ru, Rh, Ir—has been explored long before [19] the present focus on the layered materials like graphene, TMDs, and Bi-based three-dimensional topological insulators. The single layer of MCl_3 consists of a Cl-M-Cl sandwich where a sheet of M atoms is sandwiched between two sheets of Cl atoms, with edge-sharing $OsCl_6$ octahedra forming a honeycomb lattice, as illustrated in Fig. 1. The weakness of van der Waals forces holding layers of MCl_3 together is illustrated in Table I where we compare their interlayer binding energy, defined as $E_b = (E_{\text{monolayer}} - E_{\text{crystal}}/n)(|\vec{a} \times \vec{b}|)^{-1}$, with that of popular layered materials like graphite and Bi_2Se_3. Here $E_{\text{monolayer}}$ is the total energy of monolayer unit cell, E_{crystal} is the total energy of a three-dimensional crystal unit cell, n is the number of layers in a three-dimensional crystal unit cell, and $|\vec{a} \times \vec{b}|$ is the area of the unit cell.

Monolayer $OsCl_3$ is *largely unexplored* among transition metal trichlorides where, e.g., monolayer $RuCl_3$ as SO-

TABLE I. Interlayer binding energy E_b (in meV/Å^2) of selected transition metal trichlorides MCl_3. For comparison, E_b of typical layered materials like graphite (note that computed value for graphite is comparable to experimental estimate $E_b = 23.3 \pm 1.9$ meV/Å^2 [20]) or Bi_2Se_3 is also included.

	$OsCl_3$	VCl_3	$FeCl_3$	$RuCl_3$	graphite	Bi_2Se_3
E_b	14.4	17.3	18.1	19.3	26.4	23.9

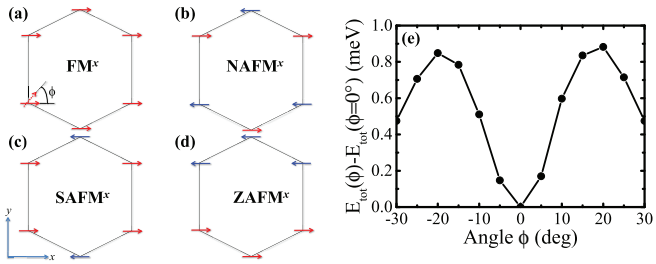

FIG. 4. Possible configurations of Os spins on the honeycomb lattice: (a) ferromagnet (FM), (b) Néel antiferromagnet (NAFM), (c) stripy AFM (SAFM), and (d) zigzag AFM (ZAFM). (e) Change of total energy $E_{\rm tot}$ as spins in FM^x configuration in (a) rotate within the xy plane.

coupled Mott insulator [21] has recently been under intense scrutiny [22] as a possible realization of the Kitaev quantum spin-liquid phase [23,24]. Nevertheless, the bulk material does exist below temperature $\lesssim 773$ K [25] and has been the subject of recent detailed x-ray spectroscopic studies [26]. By computing the phonon band structure of monolayer $OsCl_3$ in the Supplemental Material (SM) [27], where it is also *important* to include SOC, we confirm the absence of imaginary frequencies thereby ensuring that its lattice structure is at least metastable.

The topologically nontrivial band structure of $OsCl_3$ is brought about by the combination of honeycomb lattice formed by Os ions, strong SOC [12] of heavy transition metal osmium atoms, and ferromagnetic ordering of their magnetic moments. Our predictions are based on DFT calculations of electronic structure of an infinite sheet of $OsCl_3$ in Fig. 2, as well as on tight-binding calculations for semi-infinite sheets where Fig. 3 confirms the presence of one chiral state per edge associated with $\mathcal{C} = -1$. While theoretical and computational searches [1,4,18] for QAH insulators have largely been focused on finding materials or heterostructures with nonzero (and as large as possible [28]) $\mathcal{C}$ characterizing their bulk band structure, we show that understanding of a variety of possible spin orderings on the honeycomb lattice [24] (see Fig. 4) or spatial and transport properties [29] of chiral edge states (see Sec. IV in the SM [27]) deserves their own attention.

In addition, motivated by the fact that comparable energy scales associated with SOC and Coulomb interaction were found to lead to a variety of competing emergent quantum phases [21,30–32] in Ir and Os oxides, we also use DFT combined with Hubbard U correction (DFT+U) [33] to investigate the effect of the on-site Coulomb repulsion of 5*d* electrons of Os. For monolayer $OsCl_3$, Fig. 2(d) unveils a transition from QAH insulator with $\mathcal{C} \neq 0$ to Mott insulator with $\mathcal{C} = 0$ as U is increased toward some critical value U_c. In Fig. 2(d) we find $U \simeq 0.35$ eV, but U_c increases with decreasing lattice spacing a (reaching $U \simeq 0.6$ eV at the likely experimental value for a [26], as discussed in Sec. II in the SM [27]).

Magnetic orderings of Os atoms. Surprisingly, despite a requirement for large SOC to open sizable E_g, studies of candidate QAH insulators often naïvely assume that their magnetization is perpendicular to the plane of a 2D electron system [1], thereby neglecting SOC-generated MCA. The MCA is fundamental property of any magnet which selects energetically favorable magnetization directions (such as easy-axis, easy-plane or easy-cone) and determines stability of that direction [12]. Moreover, MCA is crucial [34] to evade the Mermin-Wagner theorem according to which $T_{\rm C} \equiv 0$ for isotropic Heisenberg ferromagnet with finite-range interactions.

TABLE II. The total energy $E_{\rm tot}$ per unit cell (in meV, relative to $E_{\rm tot}$ of FM^x ground state), as well as spin $\langle S\rangle$ and orbital $\langle O\rangle$ moments (in μ_B), for several magnetic configurations of Os atoms (first four of which are illustrated in Fig. 4) calculated by GGA+SOC method. Paramagnetic state has $E_{\rm tot} = 47.36$ meV and $\langle S\rangle = \langle O\rangle = 0$.

	FM^x	NAFM^x	SAFM^x	ZAFM^x	FM^z	FM^y	NAFM^y
$E_{\rm tot}$	0.0	39.60	47.57	16.63	27.42	0.51	39.61
$\langle S\rangle$	0.57	0.13	0.10	0.41	0.30	0.57	0.13
$\langle O\rangle$	0.30	0.24	0.90	0.33	0.12	0.30	0.24

Since in-plane magnetization or magnetic field cannot by itself induce quantized Hall conductance, some studies of potential QAH insulators have proposed [12] to apply external electric field to change MCA energy so that easy-axis tilts out of the plane. However, even *in-plane magnetization* can generate QAH effect in crystals with preserved inversion symmetry but broken out-of-plane mirror reflection symmetry (i.e., $z \to -z$) [35], as satisfied by the lattice shown in Fig. 1. Another important issue is that ferromagnetic ordering, where all spins point in or out of the plane of $OsCl_3$, might not be the ground state of magnetic moments residing on the sites of the honeycomb lattice [24].

Therefore, prior to analyzing electronic band structure of monolayer $OsCl_3$, we first investigate total energy $E_{\rm tot}$ of four possible in-plane magnetic configurations shown in Fig. 4(a), as well as of the ferromagnetic one where spins point out of the plane (FM^z) and the paramagnetic (PM) one. Table II shows that ferromagnetic configuration FM^x, whose spins point along the x axis, is the ground state (even at finite U, see Fig. S3 in the SM [27]). Additionally, Fig. 4(b) shows that energy $E_{\rm tot}$ increases if Os spins try to move away from the x axis as the easy axis. This means that monolayer $OsCl_3$ is an anisotropic 2D XY ferromagnet [36], or, more precisely, "planar rotator" [37] ferromagnet as a special case of 2D XY model where $S_z \equiv 0$. Its spin-spin interactions are described by an effective Hamiltonian $H_\parallel = -\sum_{\langle ij\rangle} J_\parallel (S_i^x S_j^x + S_i^y S_j^y) - \sum_i D(S_i^x)^2$, where (S_x, S_y) is the spin operator in quantum [36] or unit vector [37] in the classical version of the model, $\langle ij\rangle$ denotes the summation over nearest neighbors, and D quantifies anisotropy ($D \to \infty$ suppresses fluctuations in the y component of the spins, thereby leading to the Ising model). The 2D system described by $H_\parallel$ with sufficiently large $D/J_\parallel$ undergoes transition from FM^x to PM at the Curie temperature which we estimate [38] as $T_{\rm C} \lesssim 350$ K for $D/J \simeq 0.4$ according to Table II and Fig. 4(b) [for $D/J \lesssim 10^{-7}$ [38], one expects transition from FM^x to Berezinskii-Kosterlitz-Thouless (BKT) phase with topological order, and then to PM at $T_{\rm BKT}$]. The interplane exchange coupling described by an additional Hamiltonian, $H_\perp = -\sum_{\langle ij\rangle} J_\perp (S_i^x S_j^x + S_i^y S_j^y)$, would further increase [37] $T_{\rm C}$ of $OsCl_3$ multilayers, whose spin Hamiltonian is given by $H_\parallel + H_\perp$ with $J_\perp/J_\parallel \simeq 0.1$ estimated from DFT calculations for $OsCl_3$ bilayer.

Topology of bulk band structure. Figures 2(a) and 2(c) show bulk band structure of monolayers $OsCl_3$ (assuming $U = 0$) in the FM^x and FM^z configuration of Os spins, respectively, computed using DFT implemented in the VASP package [39]. The electron core interactions are described by the projector augmented wave (PAW) method [40], and we use Perdew-Burke-Ernzerhof parametrization of generalized gradient approximation (GGA) for the exchange-correlation functional. The cutoff energy for the plane wave basis set is 500 eV for all calculations. The k-point mesh $10 \times 10 \times 1$ is used for the Brillouin zone integration in the self-consistency cycle. For the density of states (DOS) and E_{tot} in Table II we use finer meshes of $25 \times 25 \times 1$ and $32 \times 32 \times 1$ points, respectively. We fully optimize the atomic coordinates until Hellmann-Feynman forces on each ion are less than 0.01 eV/Å, which yields the lattice constant $a_0 = 5.99$ Å (note that a recent x-ray study finds $a = 5.87$ Å [26]).

When SOC is switched off, Fig. 2(a) shows that monolayer $OsCl_3$ exhibits nonzero exchange splitting between spin-up and spin-down bands, but remains metallic. Switching SOC on opens a band gap $E_g \simeq 67$ meV around E_F, as highlighted by the DOS in Fig. 2(b). Furthermore, this gap is topologically nontrivial as indicated by the nonzero Chern number, $\mathcal{C} = -1$ (note that we find $\mathcal{C} = 3$ for VCl_3 and $\mathcal{C} = -1$ for $RuCl_3$, but $\mathcal{C} = 0$ for $FeCl_3$, $CoCl_3$, and $IrCl_3$). Figure 2(c) shows that $E_g \simeq 191$ meV would be even larger for FM^z configuration of spins, but this requires us to apply a very large out-of-plane electric field due to the large difference between E_{tot} of FM^x and FM^z configurations in Table II. The Chern number $\mathcal{C} = 1$ is obtained for FM^z configuration of spins in Fig. 2(c), which also shows how $\mathcal{C}$ could increase [28] by tuning E_F (such as by gate voltage [41]) into different gaps of the bulk band structure in Fig. 2(c).

We compute $\mathcal{C}$ from the Kubo formula [42] using the k-space Hamiltonian obtained by Fourier transforming the real-space tight-binding Hamiltonian (TBH) in the basis of maximally localized Wannier functions [43]. Since low-energy physics is mainly dominated by 5d orbitals of transition-metal atoms, we use all five d orbitals centered on each Os atom, while p orbitals on Cl atoms are neglected. The on-site potential and hopping through the fourth-nearest neighbor are calculated directly from the GGA+SOC Hamiltonian generated by DFT calculations. Moreover, the DOS in Fig. 2(b) shows that the crystal field splits d orbitals into t_{2g} and e_g, where only three t_{2g} orbitals contribute to the DOS around E_F (whereas the contribution of p orbitals of Cl is much smaller).

Energy-momentum dispersion of chiral edge state. We also use Wannier TBH to obtain the local DOS at the zigzag or armchair edge of a sheet of $OsCl_3$ which is infinite in the x direction and semi-infinite in the y direction. The local DOS, computed from the retarded Green function as $-\text{Im}\,\hat{G}^r(E; k_x, j)/\pi$ [44], is plotted in Fig. 3. It confirms the presence of one chiral edge state, whose E-k_x dispersion penetrates through the E_g gap, in accord with $|\mathcal{C}| = 1$ and *bulk-boundary correspondence* [45]. The spatial and quantum transport properties of chiral edge states in $OsCl_3$ nanoribbons with different edge termination, including the role of the kink [45] in E-k_x dispersion in Fig. 3(c) on the transmission function in the presence of disorder, are discussed in the SM [27].

Correlation-driven topological quantum phase transition. Although the accurate value of U is not known for $OsCl_3$, we expect moderate correlation effects due to spatially extended 5d orbitals of Os. Therefore, similarly to recent studies of electronic phases in other Os compounds [32] we vary U from 0 to 1.5 eV in Fig. 2(d), with effective $U = U' - J$ chosen in Dudarev parametrization of DFT+U where the exchange parameter J is not treated separately. This reveals that the QAH insulating phase persists up to some critical value $U_c \simeq 0.35$ eV (for its dependence on the lattice constant see the SM [27]), at which $E_g \to 0$ due to electron correlations. Further increase of $U > U_c$ opens a gap of SO-coupled Mott insulating phase which is topologically trivial with $\mathcal{C} = 0$. Thus, transition from QAH insulator to Mott insulator is an example of a continuous (due to gap closing at U_c) topological (due to change of topological number $\mathcal{C}$) quantum phase transition [46].

Conclusions. Using DFT and DFT+U, as well as MCA energy and quantum transport, calculations we predict that monolayer $OsCl_3$ offers an unforeseen playground to examine electronic phases governed by the *interplay between SOC, low-dimensional magnetism stabilized by large anisotropy due to strong SOC, and correlations of* 5d *electrons*. Upon increasing the on-site Coulomb repulsion, monolayer $OsCl_3$ undergoes a quantum phase transition from QAH insulator to correlated metal and finally to topologically trivial SO-coupled Mott insulator. Interestingly, a large gap $E_g = 67$ meV with nonzero Chern number $\mathcal{C} = -1$ is observed even though its spontaneous magnetization is along the in-plane easy axis, which is possible when the mirror reflection symmetry is broken [35]. We note that Ref. [31] has proposed a heuristic phase diagram in which the QAH insulating phase borders [28] a trivial Mott insulator. Thus, our Fig. 2(d) can be viewed as a prescription for realizing such phase diagrams by using realistic materials whose 2D nature makes it possible to manipulate its charge density and E_F by the gate electrode (as demonstrated very recently in correlated monolayer TMDs [41]). The correlations of 5d electrons characterized by spatially extended wave functions can be captured more accurately with DFT+dynamical mean field theory [47], which we relegate to future studies.

Acknowledgements. We thank Jiadong Zang for valuable insights. This work was supported by NSF Grant No. ECCS 1509094. The supercomputing time was provided by XSEDE, which is supported by NSF Grant No. ACI-1053575.

[1] C.-X. Liu, S.-C. Zhang, and X.-L. Qi, Annu. Rev. Condens. Matter Phys. **7**, 301 (2016).

[2] X. Kou, Y. Fan, M. Lang, P. Upadhyaya, and K. L. Wang, Solid State Commun. **215–216**, 34 (2015).

[3] C. L. Kane and E. J. Mele, Phys. Rev. Lett. **95**, 226801 (2005).

[4] K. Dolui, S. Ray, and T. Das, Phys. Rev. B **92**, 205133 (2015).

[5] Z. Qiao, W. Ren, H. Chen, L. Bellaiche, Z. Zhang, A. H. MacDonald, and Q. Niu, Phys. Rev. Lett. **112**, 116404 (2014).

[6] J. Zhang, B. Zhao, Y. Yao, and Z. Yang, Phys. Rev. B **92**, 165418 (2015).

[7] F. D. M. Haldane, Phys. Rev. Lett. **61**, 2015 (1988).
[8] S.-C. Wu, G. Shan, and B. Yan, Phys. Rev. Lett. **113**, 256401 (2014).
[9] D. Xiao, W. Zhu, Y. Ran, N. Nagaosa, and S. Okamoto, Nat. Commun. **2**, 596 (2011).
[10] C. Weeks, J. Hu, J. Alicea, M. Franz, and R. Wu, Phys. Rev. X **1**, 021001 (2011).
[11] M. Gmitra, D. Kochan, P. Högl, and J. Fabian, Phys. Rev. B **93**, 155104 (2016).
[12] H. Zhang, C. Lazo, S. Blügel, S. Heinze, and Y. Mokrousov, Phys. Rev. Lett. **108**, 056802 (2012).
[13] Z. Wang, C. Tang, R. Sachs, Y. Barlas, and J. Shi, Phys. Rev. Lett. **114**, 016603 (2015).
[14] X.-L. Zhang, L.-F. Liu, and W.-M. Liu, Sci. Rep. **3**, 2908 (2013).
[15] D. Doennig, S. Baidya, W. E. Pickett, and R. Pentcheva, Phys. Rev. B **93**, 165145 (2016).
[16] A. Cresti, D. V. Tuan, D. Soriano, A. W. Cummings, and S. Roche, Phys. Rev. Lett. **113**, 246603 (2014).
[17] P.-H. Chang, M. S. Bahramy, N. Nagaosa, and B. K. Nikolić, Nano Lett. **14**, 3779 (2014).
[18] G. Xu, B. Lian, and S.-C. Zhang, Phys. Rev. Lett. **115**, 186802 (2015).
[19] H. Bengel, H.-J. Cantow, S. N. Maganov, H. Hillebrecht, G. Thiele, W. Liang, and M.-H. Whangbo, Surf. Sci. **343**, 95 (1995).
[20] R. Zacharia, H. Ulbricht, and T. Hertel, Phys. Rev. B **69**, 155406 (2004).
[21] J. G. Rau, E. K.-H. Lee, and H.-Y. Kee, Annu. Rev. Condens. Matter Phys. **7**, 195 (2016).
[22] A. Banerjee, C. A. Bridges, J.-Q. Yan, A. A. Aczel, L. Li, M. B. Stone, G. E. Granroth, M. D. Lumsden, Y. Yiu, J. Knolle, S. Bhattacharjee, D. L. Kovrizhin, R. Moessner, D. A. Tennant, D. G. Mandrus, and S. E. Nagler, Nat. Mater. **15**, 733 (2016).
[23] G. Jackeli and G. Khaliullin, Phys. Rev. Lett. **102**, 017205 (2009).
[24] C. C. Price and N. B. Perkins, Phys. Rev. Lett. **109**, 187201 (2012).
[25] I. L. Shabalin, *Ultra-High Temperature Materials I: Carbon (Graphene/Graphite) and Refractory Metals* (Springer, Berlin, 2014).
[26] K. A. Lomachenko, C. Garino, E. Gallo, D. Gianolio, R. Gobetto, P. Glatzel, N. Smolentsev, G. Smolentsev, A. V. Soldatov, C. Lamberti, and L. Salassa, Phys. Chem. Chem. Phys. **15**, 16152 (2013).
[27] See Supplemental Material (which includes Refs. [48–53]) at http://link.aps.org/supplemental/10.1103/PhysRevB.95.201402 for the analysis of: phonon band structure of $OsCl_3$ in the presence and absence of SOC (Sec. I), lattice spacing dependence of the critical value of Hubbard U_c (Sec. II), E_{tot} of different magnetic configurations as a function of increasing Hubbard U (Sec. III), and spatial and transport properties of chiral edge states in zigzag and armchair nanoribbons made of $OsCl_3$ in the QAH insulator phase (Sec. IV).
[28] Y.-J. Song, K.-H. Ahn, W. E. Pickett, and K.-W. Lee, Phys. Rev. B **94**, 125134 (2016).
[29] J. Wang, B. Lian, H. Zhang, and S.-C. Zhang, Phys. Rev. Lett. **111**, 086803 (2013).
[30] X. Wan, A. M. Turner, A. Vishwanath, and S. Y. Savrasov, Phys. Rev. B **83**, 205101 (2011).
[31] W. Witczak-Krempa, G. Chen, Y. B. Kim, and L. Balents, Annu. Rev. Condens. Matter Phys. **5**, 57 (2014).
[32] X. Wan, A. Vishwanath, and S. Y. Savrasov, Phys. Rev. Lett. **108**, 146601 (2012).
[33] V. I. Anisimov, F. Aryasetiawan, and A. I. Lichtenstein, J. Phys.: Condens. Matter **9**, 767 (1997).
[34] K. Binder and D. P. Landau, Phys. Rev. B **13**, 1140 (1976).
[35] Y. Ren, J. Zeng, X. Deng, F. Yang, H. Pan, and Z. Qiao, Phys. Rev. B **94**, 085411 (2016); Y. Ren, Z. Qiao, and Q. Niu, Rep. Prog. Phys. **79**, 066501 (2016).
[36] Y.-Q. Ma and W. Figueiredo, Phys. Rev. B **55**, 5604 (1997).
[37] B. V. Costa, A. R. Pereira, and A. S. T. Pires, Phys. Rev. B **54**, 3019 (1996).
[38] D. V. Spirin and Yu. A. Fridman, Physica B **325**, 410 (2003).
[39] G. Kresse and J. Hafner, Phys. Rev. B **47**, 558 (1993); G. Kresse and J. Furthmüllerb, Comput. Mater. Sci. **6**, 15 (1996).
[40] P. E. Blöchl, Phys. Rev. B **50**, 17953 (1994); G. Kresse and D. Joubert, *ibid.* **59**, 1758 (1999).
[41] L. J. Li, E. C. T. O'Farrell, K. P. Loh, G. Eda, B. Özyilmaz, and A. H. C. Neto, Nature (London) **529**, 185 (2016); Y. Yu, F. Yang, X. F. Lu, Y. J. Yan, Y.-H Cho, L. Ma, X. Niu, S. Kim, Y.-W. Son, D. Feng, S. Li, S.-W. Cheong, X. H. Chen, and Y. Zhang, Nat. Nanotechnol. **10**, 270 (2015).
[42] D. J. Thouless, M. Kohmoto, M. P. Nightingale, and M. den Nijs, Phys. Rev. Lett. **49**, 405 (1982).
[43] N. Marzari, A. A. Mostofi, J. R. Yates, I. Souza, and D. Vanderbilt, Rev. Mod. Phys. **84**, 1419 (2012); A. A. Mostofi, J. R. Yates, Y.-S. Lee, I. Souza, D. Vanderbilt, and N. Marzari, Comp. Phys. Commun. **178**, 685 (2008).
[44] H. Zhang, C.-X. Liu, X.-L. Qi, X. Dai, Z. Fang, and S.-C. Zhang, Nat. Phys. **5**, 438 (2009).
[45] C. Kane, in *Contemporary Concepts of Condensed Matter Science* Volume 6, edited by M. Franz and L. Molenkamp (Elsevier, Amsterdam, 2013).
[46] B. Roy, P. Goswami, and J. D. Sau, Phys. Rev. B **94**, 041101 (2016); A. Amaricci, J. C. Budich, M. Capone, B. Trauzettel, and G. Sangiovanni, *ibid.* **93**, 235112 (2016).
[47] K. Held, Adv. Phys. **56**, 829 (2007).
[48] A. Togo, F. Oba, and I. Tanaka, Phys. Rev. B **78**, 134106 (2008).
[49] M. Cococcioni and S. de Gironcoli, Phys. Rev. B **71**, 035105 (2005).
[50] S. Datta, *Electronic Transport in Mesoscopic Systems* (Cambridge University Press, Cambridge, 1995).
[51] T. O. Wehling, A. M. Black-Schaffer, and A. V. Balatsky, Adv. Phys. **63**, 1 (2014).
[52] A. Ferreira and E. R. Mucciolo, Phys. Rev. Lett. **115**, 106601 (2015).
[53] E. Prada and G. Metalidis, J. Comp. Electron. **12**, 63 (2013).

Supplemental Material for "Monolayer of $5d$ transition metal trichloride $OsCl_3$: A playground for two-dimensional magnetism, room temperature quantum anomalous Hall effect and topological phase transitions"

Xian-Lei Sheng[1,2] and Branislav K. Nikolić[1,*]

[1]*Department of Physics and Astronomy, University of Delaware, Newark, DE 19716-2570, USA*
[2]*Department of Applied Physics, Beihang University, Beijing 100191, China*

In this Supplemental Material we provide additional results for: phonon band structure of $OsCl_3$ in the presence and absence of SOC which allows to examine stability of monolayer $OsCl_3$ (Sec. I); lattice spacing dependence of the critical value of Hubbard U_c (Sec. II); total energy $E_{\rm tot}$ of different magnetic configurations as a function of increasing Hubbard U (Sec. III); and spatial and transport properties of chiral edge states in zigzag and armchair nanoribbons made of $OsCl_3$ in the QAH insulator phase with $U = 0$ (Sec. IV).

I. PHONON BAND STRUCTURE IN THE PRESENCE AND ABSENCE OF SPIN-ORBIT COUPLING

Figure S1 shows phonon band structure of monolayer $OsCl_3$. Since the effect of spin-orbit coupling (SOC) on phonons can be profound on surfaces and in thin films of materials containing heavy elements, Fig. S1 plots phonon frequency-momentum dispersion in the presence of SOC and FM^x magnetic ordering from Fig. 4(a) of the main text. Comparing this result (dashed line in Fig. S1) with phonon band structure of monolayer $OsCl_3$ where SOC is artificially turned off (solid line in Fig. S1), indeed confirms the importance of including SOC in phonon calculations. In both cases, we find no imaginary frequencies, which ensures that the lattice structure of monolayer $OsCl_3$ is at least metastable. We note that in the paramagnetic monolayer $OsCl_3$ without SOC, whose energy in Table II of the main text is much higher than the ground state with FM^x ordering and SOC, we do find some imaginary phonon frequencies.

The phonon calculations were performed on the primitive unit cell using density functional perturbation theory as implemented within the `VASP` and `PHONOPY` [1] packages. The details of `VASP` calculations are the same as in the main text, but with the cutoff energy for the plane wave basis set chosen as 400 eV and a mesh of $5 \times 5 \times 1$ used for k-point sampling. The electronic self-consistent convergence parameter was set at 1×10^{-8} eV.

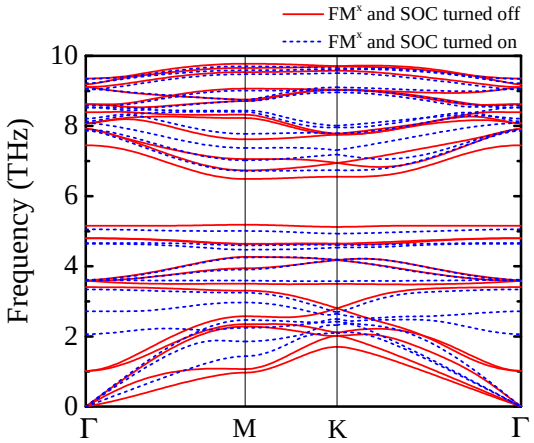

Fig. S1: The phonon band structure of monolayer $OsCl_3$ with *both* SOC and FM^x magnetic ordering from Fig. 4(a) in the main text included (dashed line). For comparison, we also show the phonon band structure in the artificial case of FM^x magnetic ordering where SOC is turned off (solid line).

*Electronic address: bnikolic@udel.edu

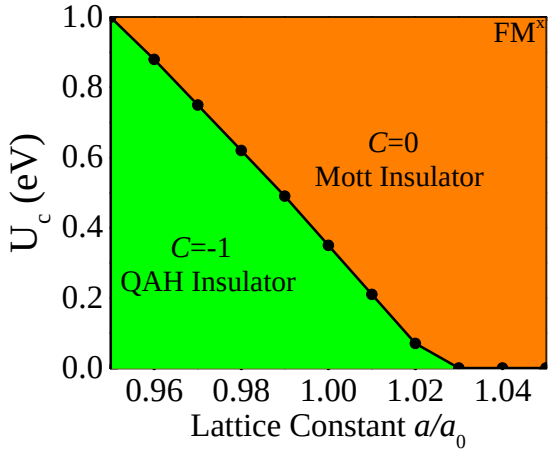

Fig. S2: Dependence of the critical value of Hubbard U_c from Fig. 2(d) in the main text on the lattice constant a of monolayer $OcCl_3$ in units of $a_0 = 5.99$ Å used in the main text.

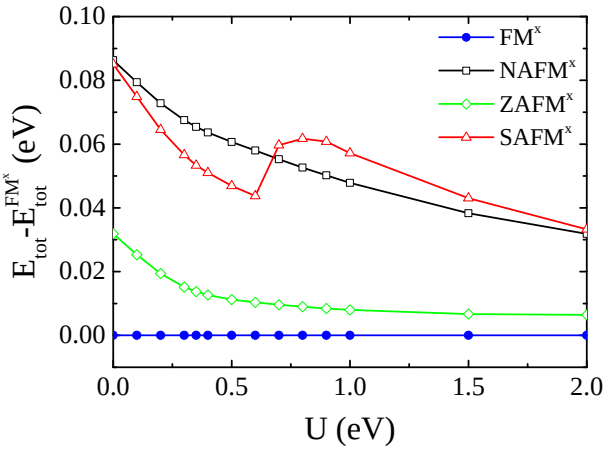

Fig. S3: The total energy $E_{\rm tot}$ per unit cell, relative to $E_{\rm tot}$ of FM^x ground state, for several magnetic configurations of Os atoms in Fig. 4 of the main text as a function of Hubbard U.

II. DEPENDENCE OF THE CRITICAL VALUE OF HUBBARD U_c ON THE LATTICE CONSTANT

Applications of DFT+U methodology to different materials have revealed sensitivity of Hubbard U on the lattice spacing of the unit cell, such as in the case of iron where a marked increase of U occurs as the lattice constant is squeezed below its experimental value [2]. In Fig. S2, we show the dependence of the critical value U_c, at which topological quantum phase transition takes place in Fig. 2(d) in the main text, on the lattice spacing. We used $a_0 = 5.99$ Å in the main text, as obtained from DFT optimization of the atomic coordinates, but the experimental lattice constant appears to be slightly smaller $a = 5.87$ Å [3] which would increase U_c from $\simeq 0.35$ eV found in Fig. 2(d) in the main text to $U_c \simeq 0.6$ eV at $a/a_0 \approx 0.98$ in Fig. S2. Although there are no extensive experimental studies of $OsCl_3$ to confirm its lattice constant obtained in Ref. [3], this estimate seems compatible with experimental lattice constants as one moves from $FeCl_3$, where $a = 6.13$ Å, to $RuCl_3$, where $a = 5.9783$ Å [4], and eventually to $OsCl_3$ with the heaviest transition metal atom among the three isoelectronic ones.

III. DEPENDENCE OF THE TOTAL ENERGY OF DIFFERENT MAGNETIC CONFIGURATIONS ON HUBBARD U

All calculations of the total energy $E_{\rm tot}$ for different magnetic configurations in Fig. 4 and Table II of the main text are performed at $U = 0$. Figure S3 shows $E_{\rm tot}$ as a function of increasing U, which demonstrates that FM^x configuration in Fig. 4(a) remain the ground state even at finite U.

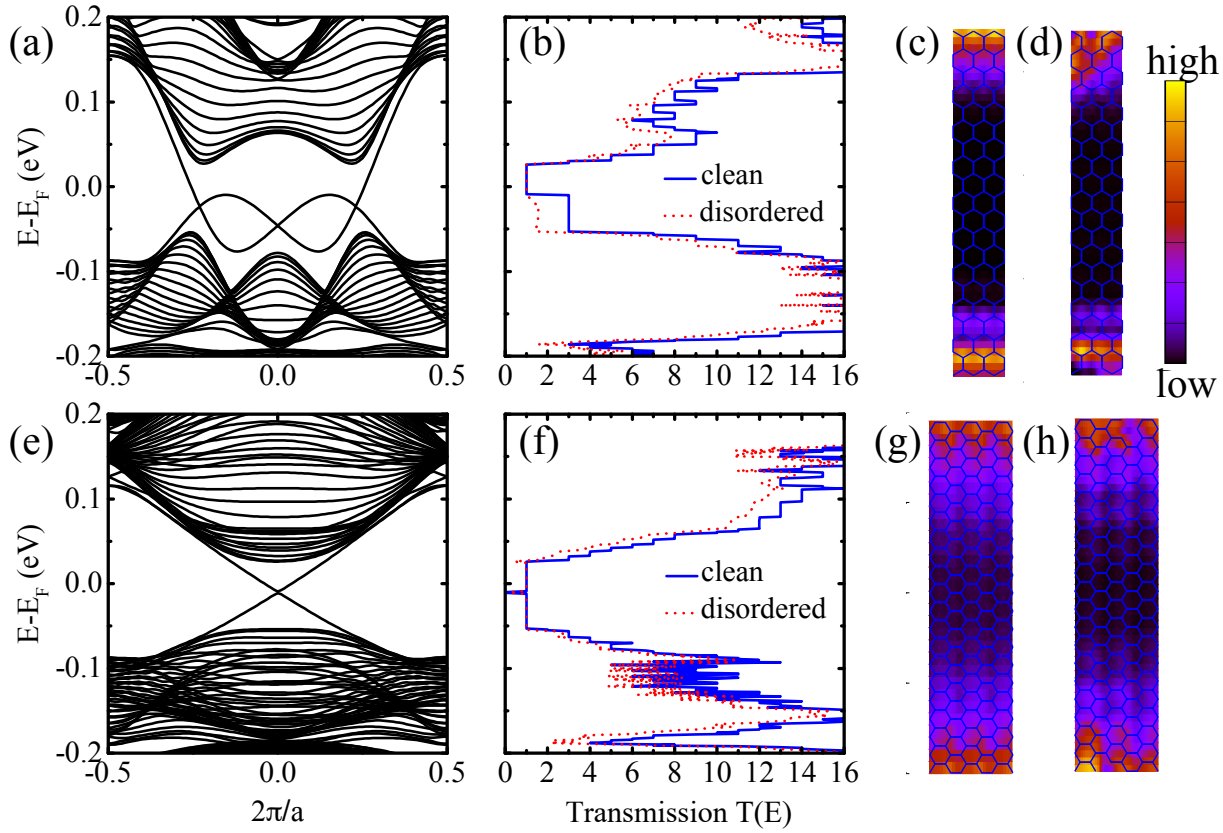

Fig. S4: Electronic subband structure of $OsCl_3$ nanoribbons for: (a) zigzag edges and width $W \simeq 10$ nm; (e) armchair edges and $W \simeq 12$ nm. The zero-bias transmission function $T(E)$ for zigzag and armchair nanoribbons, which are clean [as in panels (a) and (e)] or disordered by one vacancy at Os site on each edge are shown in panels (b) and (f), respectively. The local DOS for zigzag (armchair) nanoribbon with and without vacancy is shown in panels (c) and (d) [(g) and (h)], respectively.

IV. SPATIAL AND QUANTUM TRANSPORT PROPERTIES OF CHIRAL EDGE STATES IN ZIGZAG AND ARMCHAIR NANORIBBONS

Using Wannier tight-binding Hamiltonian discussed in the main text, we compute the real-space retarded Green function [7]

$$\hat{G}^r(E;i,j) = [E - \hat{H} - \hat{\Sigma}^r_L - \hat{\Sigma}^r_R]^{-1} \tag{1}$$

of the central region of $OsCl_3$ nanoribbons attached to the left (L) and right (R) semi-infinite leads of the same width W. The leads generate self-energies $\hat{\Sigma}^r_{L,R}$ determining escape rates of electrons from the central region into the macroscopic reservoirs kept at electrochemical potential $\mu_{L,R}$. The active region is either perfectly clean or host two vacancies (one on each edge) as defects obtained by cutting out all bonds adjacent to a chosen Os site. For example, in Dirac materials like graphene and Bi_2Se_3 vacancies drastically affect the local DOS, by introducing sharp peaks of quasilocalized character which can be detected by scanning tunneling microscopy [8], and represent infinitely strong scatterers which cannot be handled by any perturbative analysis [9].

The subband structure of clean zigzag and armchair nanoribbons is shown in Figs. S4(a) and S4(e), respectively. Using the retarded Green function and the level broadening function $\hat{\Gamma}_{L,R} = -2\mathrm{Im}[\hat{\Sigma}^r_{L,R}]$, we compute the transmission function [7]

$$T(E) = \mathrm{Tr}[\hat{\Gamma}_R \hat{G}^r \hat{\Gamma}_L (\hat{G}^r)^\dagger] \tag{2}$$

at vanishing applied bias voltage $\mu_L - \mu_R \to 0$, which is plotted in Figs. S4(b) and S4(f). It exhibits quantized steps in the clean case, which are destroyed outside of the bulk gap region in Figs. S4(a) and S4(e) when vacancies are introduced. However, $T(E)$ in Fig. S4(f) has a dip even within the topologically protected bulk gap due to wide spatial extension of edge states in the armchair case, so that hybridization of edge states from opposite edges opens

a minigap at the crossing point in Fig. S4(e). The local DOS, $-\mathrm{Im}\,\hat{G}^r(E;i,i)/\pi$, shown for zigzag in Fig. S4(c) and armchair nanoribbons in Fig. S4(g) confirms that edge states in the former case are narrower than in the latter case, as observed previously [5, 6] for edge states of QSH insulators emerging from different types of graphene nanoribbons.

The zigzag edge changes the Hamiltonian near the boundary which then introduces a kink in the dispersion of edge state in Figs. 3(c) of the main text and S4(a), as also found for the Haldane model defined on the honeycomb lattice with zigzag edge [10]. For some values of energy E within the bulk band gap, such dispersion intersect with E at $N_R = 2$ points with positive velocity and $N_L = 1$ points with negative velocity. This leads to $T(E) = 3$ for E within a portion of the bulk band gap in Fig. S4(b). Nevertheless, only the difference $N_R - N_L = |\mathcal{C}|$ is topologically protected according to *bulk-boundary correspondence* [10], leading to $T(E) \geq 1$ across the whole bulk band gap even in the presence of vacancies in Fig. S4(b).

[1] A. Togo, F. Oba, and I. Tanaka, Phys. Rev. B **78**, 134106 (2008).
[2] M. Cococcioni and S. de Gironcoli, Phys. Rev. B **71**, 035105 (2005).
[3] K. A. Lomachenko *et. al.*, Phys. Chem. Chem. Phys. **15**, 16152 (2013).
[4] A. Banerjee *et al.*, Nat. Mater. doi:10.1038/nmat4604 (2016).
[5] P.-H. Chang, M. S. Bahramy, N. Nagaosa, and B. K. Nikolić, Nano Lett. **14**, 3779 (2014).
[6] E. Prada and G. Metalidis, J. Comp. Electron. **12**, 63 (2013).
[7] S. Datta, *Electronic transport in mesoscopic systems* (Cambridge University Press, Cambridge, 1995).
[8] T. O. Wehling, A. M. Black-Schaffer, and A. V. Balatsky, Adv. Phys. **76**, 1 (2014).
[9] A. Ferreira and E. R. Mucciolo, Phys. Rev. Lett. **115**, 106601 (2015).
[10] C. Kane, in *Contemporary Concepts of Condensed Matter Science Volume 6*, edited by M. Franz and L. Molenkamp (Elsevier, Amsterdam, 2013).